

# Passive Synthetic Aperture Hitchhiker Imaging of Ground Moving Targets - Part 1: Image Formation and Velocity Estimation

Steven Wacks *Student Member, IEEE* and Birsen Yazıcı\*, *Senior Member, IEEE*

## Abstract

In the Part 1 of this two-part study, we present a method of imaging and velocity estimation of ground moving targets using passive synthetic aperture radar. Such a system uses a network of small, mobile receivers that collect scattered waves due to transmitters of opportunity such as commercial television, radio, and cell phone towers. Therefore, passive imaging systems have significant cost, manufacturing, and stealth advantages over active systems.

We describe a novel generalized Radon transform type forward model and a corresponding filtered-backprojection type image formation and velocity estimation method. We form a stack of position images over a range of hypothesized velocities, and show that the targets can be reconstructed at the correct position whenever the hypothesized velocity is equal to the true velocity of targets. We then use entropy to determine the most accurate velocity and image pair for each moving target. We present extensive numerical simulations to verify the reconstruction method.

Our method does not require a priori knowledge of transmitter locations and transmitted waveforms. It can determine the location and velocity of multiple targets moving at different velocities. Furthermore, it can accommodate arbitrary imaging geometries. In Part 2, we present the resolution analysis and analysis of positioning errors in passive SAR images due to erroneous velocity estimation.

## I. INTRODUCTION

### A. Motivation

A hitchhiker is a passive radar receiver that uses sources of opportunity instead of a dedicated transmitter [1]–[8]. The rapid growth of radio, cell phone, and television transmission towers provides ample opportunities for these hitchhikers to perform radar tasks. Additionally, the absence of active signal propagation from the system provides key advantages such as cost, simplicity of implementation, and stealth.

Copyright (c) 2013 IEEE. Personal use of this material is permitted. However, permission to use this material for any other purposes must be obtained from the IEEE by sending a request to pubs-permissions@ieee.org.

This work was supported by the Air Force Office of Scientific Research (AFOSR) under the agreements FA9550-09-1-0013 and FA9550-12-1-0415, and by the National Science Foundation (NSF) under grants CCF-08030672 and CCF-1218805.

Wacks and Yazici are with the Department of Electrical, Computer and Systems Engineering, Rensselaer Polytechnic Institute, 110 8th Street, Troy, NY 12180 USA E-mail: yazici@ecse.rpi.edu, wackss@rpi.edu, Phone: (518)-276 2905, Fax: (518)-276 6261

\*Corresponding author

Synthetic aperture radar (SAR) image formation methods are typically designed for imaging stationary scenes, and reconstructing scenes with moving targets is a challenging task. These moving targets appear smeared and unfocused in reconstructed images. Many methods have been presented in the literature that attempt to address the problem of SAR imaging of ground moving targets (SAR/GMTI) [9]–[20]. Synthetic aperture hitchhiker imaging of ground moving targets (SAH/GMTI) involves high resolution position and velocity estimation of a scene using transmitters of opportunity and multiple moving receivers. The transmitters of opportunity can be cooperative where the location of transmitters and transmitted waveforms are known or non-cooperative where no such information is available.

In this paper, we develop a novel forward model and a corresponding image formation method to reconstruct both the scene reflectivity and the two-dimensional velocity of multiple moving targets using non-cooperative sources of opportunity. Our method extends the passive imaging of stationary scene that we presented in [6].

### *B. Related Work*

To the best of our knowledge, no work has been published to address the problem of passive synthetic aperture radar imaging of ground moving targets using non-cooperative sources of opportunity. However, literature on passive SAR imaging of stationary scenes using non-cooperative sources of opportunity can be found in [6]–[8]. In [6], an image reconstruction method is developed using filtered backprojection (FBP) on data correlated between the receivers to image a stationary scene. Similarly, [7], [8] present methods of passive SAR imaging of a stationary scene, but using ultra-narrowband waveforms of opportunity.

Several recent studies reported on passive imaging of moving and stationary scenes using cooperative sources of opportunity [21]–[23]. These methods rely on collecting the direct path signal from a transmitter of opportunity and using this signal in conventional bistatic radar imaging mode. In [24], a passive bistatic radar experiment is conducted using an airborne receiver attempting to detect airborne targets. The algorithm employed direct path signal suppression followed by a constant false alarm rate detection scheme.

In addition to passive SAR imaging of a stationary scene, there has been work published on passive radar imaging of moving targets with stationary receivers using both cooperative and non-cooperative sources of opportunity [1]–[5], [25]–[30]. For example, [29] uses a sparse array of stationary receivers to take advantage of transmitting sources of opportunity to image moving targets. [1], [2], [31]–[40] investigate the properties of passive radar and look at the potential performance one can obtain from such a system. [3]–[5] all show image reconstruction methods for passive imaging of airborne targets with stationary receivers. [5] uses the simplest algorithm, direct Fourier reconstruction, to establish a lower bound and show the viability of passive imaging. [3] and [4] improve on the performance of the direct Fourier reconstruction by applying CLEAN deconvolution and region-enhanced image formation techniques, respectively.

On the other hand, SAR/GMTI with active transmitters has an extensive research base. Additionally, some systems may be called passive in a cooperative case, when the transmitter position and waveform is known. Papers that have studied this problem generally either focus on detecting the moving targets either independently or for use with other

image formation techniques, or they focus on the image formation process itself. For example, [9] and [10] focus on the target detection. [9] performs the detection in multichannel SAR using displaced phase center antenna (DPCA) and along-track interferometry (ATI) techniques, which suppress clutter by either subtracting signals from two channels or multiplying the complex conjugates, respectively. [10] performs the detection by using time-frequency analysis to estimate Doppler information for the moving target. In addition to DPCA and ATI, space-time adaptive processing is an important, well-known technique primarily used for clutter suppression, and is described in [41]–[43]. Examples of works that focus on image formation are [17] and [18]. [17] performs a keystone transform to correct for the linear migration, and [18] performs a two-dimensional matched filtering operation to produce a focused image of the moving target.

Another technique used in SAR/GMTI is to form images using hypothesized motion parameters and subsequently perform detection and estimation from this stack or sequence of images. In [11], a stack of images is created by hypothesizing a range of velocities for the target. The target can then be detected in this stack since it will be focused in one of the correct velocity images. Alternatively, a measure of focus of the image has been used to determine the accuracy of a hypothesized parameter [44]–[51]. With accurately estimated motion parameters, the reconstructed images should be maximally focused, and the contrast should be at its maximum. These papers propose various techniques to iterate and alter the image and parameters until the reconstructed image is sufficiently focused.

### *C. Overview and Advantages of Our Work*

Part 1 of this study presents a method of imaging ground moving targets using a network of airborne receivers and non-cooperative transmitters of opportunity. A novel forward model is formed by correlating the received signal between pairs of receivers. This forward model can be viewed as a generalized Radon transform where the weighted/filtered function of interest is projected onto warped passive iso-range contours that are determined by target velocities and imaging geometry. We develop a corresponding filtered backprojection (FBP) type approximate inverse and form a stack of position images, each one corresponding to a fixed velocity for a range of hypothesized velocities. We show that when the hypothesized velocity is equal to the true velocity of a target, the backprojection operator puts the target at the correct position in the reconstructed image. We design the filter so that the target is at the correct strength whenever the hypothesized velocity is equal to the true velocity of the target. Next, we use entropy as a measure of focus to determine the accuracy of the hypothesized velocity and to estimate the correct target velocities. We present numerical simulations to demonstrate the performance of the method in imaging multiple moving targets at different velocities. Although our method does not consider clutter explicitly, the simulation study shows that the image formation and entropy based velocity estimation are robust at moderate signal-to-noise and signal-to-clutter ratios.

In addition to the advantages provided by a passive system using non-cooperative transmitters of opportunity, our method provides several advantages over other SAR moving target imaging methods. The FBP method for image reconstruction uses a two-dimensional vector for the hypothesized velocity. Therefore, the method has the ability to reconstruct both components of the velocity of moving targets instead of only a single component. Another

advantage of our method is that there is no assumption of a single target; instead, multiple moving targets moving at different velocities can be reconstructed. Additionally, stationary components of the scene are not filtered, so both stationary and moving targets may be reconstructed simultaneously. Our work does not require prior information about the motion parameters of moving targets. The images and focus measure together provide the detection and estimation capability of moving targets and their motion parameters. The method can be numerically implemented efficiently with roughly the computational complexity of fast-backprojection algorithms [52]. Finally, the forward model and inversion method make no assumptions about receiver flight trajectories or the ground topography; therefore, our method applies to arbitrary imaging geometries.

In Part 2 of this study, we present a performance analysis of the inversion and velocity estimation methods developed in this paper. In particular, we present the position and velocity analysis of our method and develop a theory to analyze and predict smearing artifacts in position images due to erroneous velocity estimation. These analysis is important for understanding the capability and limitations of our method as well as designing a system that yields the best performance possible.

#### D. Organization of the Paper

The organization of the remainder of the paper is as follows: In Section II we introduce the models for a moving target and the signal scattered from a moving scene. Then, in Section III, we develop the forward model for passive SAR/GMTI. In Section IV, we develop the FBP-type image formation method for reconstruction of position images entropy-based velocity estimation method. Section V details the step-by-step procedure of the algorithm and analyzes its computational complexity. In Section VI, we present numerical simulations to illustrate the theoretical results and to demonstrate the robustness of our method in noise and clutter. Section VII concludes the paper.

## II. MOVING TARGET AND RECEIVED SIGNAL MODELS

Throughout the paper, we will use bold non-italic fonts to denote vectors in 3D, bold italic fonts to denote 2D vectors, and non-bold italic fonts to denote scalar quantities, i.e.,  $\mathbf{x} = [x_1, x_2, x_3] \in \mathbb{R}^3$ ,  $\mathbf{x} = [x_1, x_2] \in \mathbb{R}^2$ ,  $x_i \in \mathbb{R}$ ,  $i = 1, 2, 3$ . We will use calligraphic letters, such as  $\mathcal{F}$  and  $\mathcal{K}$  to denote operators.

We let  $\mathbf{x}$  be a location on the ground where  $\mathbf{x} = [\mathbf{x}, \psi(\mathbf{x})] \in \mathbb{R}^3$ ,  $\mathbf{x} \in \mathbb{R}^2$ , and  $\psi : \mathbb{R}^2 \rightarrow \mathbb{R}$  is a known smooth function for the ground topography. Since the scattering takes place in a thin region near the surface and does not penetrate deep into the ground, the reflectivity function  $V(\mathbf{x})$  is of the form

$$V(\mathbf{x}) = \rho(\mathbf{x})\delta(x_3 - \psi(\mathbf{x})), \quad (1)$$

with  $\rho(\mathbf{x})$  representing the 2D surface reflectivity of a point on the ground.

#### A. Model for the Moving Target

We now model the scatterers as moving targets and their position  $\mathbf{z}$  as a function of time. We denote  $s \in \mathbb{R}$  as the *slow-time*, which indexes each “data processing window.” Additionally, we make the start-stop approximation

for both the moving targets and receiving antennas. The start-stop approximation on the receiving antennas assumes that the range variation during a pulse reception is negligible compared to the range variation between each pulse. Similarly, the start-stop approximation on the moving targets assumes that the range variation due to the movement of the targets is negligible during a pulse reception as compared to the range variation between each pulse. Without loss of generality, we let  $\mathbf{x}$  be the position of the targets at the beginning of time ( $s = 0$ ), i.e, the beginning of the synthetic aperture. Using the assumption of constant velocity for each moving target throughout the synthetic aperture, we represent the trajectory of a scatterer by

$$\mathbf{z}(s) = \mathbf{x} + \mathbf{v}_{\mathbf{x}}s, \quad (2)$$

where  $\mathbf{v}_{\mathbf{x}}$  is the velocity of a particular point scatterer located at point  $\mathbf{x}$  when  $s = 0$ . Note that the linear target motion model may limit the length of each receiver aperture or coherent processing interval (CPI). However, as described in Section IV-A, the use of multiple receiver apertures may compensate for the effect of a short CPI. Since the targets are all located on the ground, and we have a known function of the ground topography, the velocity of the scatters  $\mathbf{v}_{\mathbf{x}}$  has the form

$$\mathbf{v}_{\mathbf{x}} = [\mathbf{v}_{\mathbf{x}}, \nabla_{\mathbf{x}}\psi(\mathbf{x}) \cdot \mathbf{v}_{\mathbf{x}}], \quad (3)$$

where  $\nabla_{\mathbf{x}}\psi(\mathbf{x}) = [\partial_{x_1}\psi(\mathbf{x}) \ \partial_{x_2}\psi(\mathbf{x})]$  is the gradient of the ground topography.

### B. Model for the Received Signal From Moving Targets

We assume that there are  $N$  receivers, each traversing a trajectory  $\gamma_i(s)$ ,  $i = 1, \dots, N$  over a scene of interest. The model derived in [53] for a moving scene describes the signal received at the  $i$ th receiver from a single, stationary transmitter located at  $\mathbf{y}$  as follows:

$$\begin{aligned} f_i(s, t) = & \int e^{-i\omega[t - (|\mathbf{x} - \gamma_i(s)| + |\mathbf{x} - \mathbf{y}|)/c_0]} \\ & \times e^{i\omega((\mathbf{x} - \gamma_i(s)) + (\mathbf{x} - \mathbf{y})) \cdot \mathbf{v}_{\mathbf{x}}s/c_0} \\ & \rho(\mathbf{x})A_i(\omega, s, \mathbf{x}, \mathbf{v}) d\omega d\mathbf{x}, \end{aligned} \quad (4)$$

where  $c_0$  is the speed of light,  $A_i(\omega, s, \mathbf{x}, \mathbf{v})$  is a slow varying amplitude term in  $\omega$  given by

$$A_i(\omega, s, \mathbf{x}, \mathbf{v}) = \frac{J_{R_i}(\omega, \mathbf{x}, s)J_T(\omega, \mathbf{x})}{(4\pi)^2|\mathbf{x} + \mathbf{v}_{\mathbf{x}}s - \gamma_i(s)||\mathbf{x} + \mathbf{v}_{\mathbf{x}}s - \mathbf{y}|}, \quad (5)$$

and includes the transmitter and receiver antenna beam patterns,  $J_T$  and  $J_{R_i}$  and the geometric attenuation factors in the denominator. Note that while  $J_{R_i}$ ,  $i = 1, \dots, N$  are known,  $J_T$ , which depends primarily on the transmitted waveform, may not be known.

## III. FORWARD MODEL

This section derives a forward model for passive synthetic aperture imaging of ground moving targets using the moving target and received signal models presented in the previous section. The forward model is based on the cross correlation of the received signal obtained at each synthetic aperture sampling interval for each pair of

receiving antennas. The radiance (position) image formation and velocity estimation will be based on the inversion of the forward model described in this section.

#### A. Cross-Receiver Correlation

Using (4) as our model for the signal received by each antenna, the cross-correlation of each pair of signals for each data processing window is

$$f_{ij}(s, \tau) = \int f_i(s, t) f_j^*(s, t - \tau) dt, \quad i, j = 1, \dots, N, \quad i \neq j, \quad (6)$$

where  $f^*$  denotes the complex conjugate of  $f$ ,  $t \in [0, T]$  is the fast-time variable for some  $T$  representing the length of the data processing window.

Note that  $A_{R_{ij}}$  includes only the known terms.

Since the reflectivity  $\rho$  and the transmitter terms are unknown we take a statistical approach and take the expected value of the correlated signal in (6). Additionally, we assume that the scene reflectivity and transmitter terms are statistically independent, and therefore,

$$E[\rho(\mathbf{x})\rho^*(\tilde{\mathbf{x}})J_T(\omega, \mathbf{x})J_T^*(\omega, \tilde{\mathbf{x}})] = E[\rho(\mathbf{x})\rho^*(\tilde{\mathbf{x}})]E[J_T(\omega, \mathbf{x})J_T^*(\omega, \tilde{\mathbf{x}})]. \quad (7)$$

Furthermore, we make the incoherent field approximation [54] and write

$$E[\rho(\mathbf{x})\rho^*(\tilde{\mathbf{x}})] = R_\rho(\mathbf{x})\delta(\mathbf{x} - \tilde{\mathbf{x}}) \quad (8)$$

where  $R_\rho$  and  $R_T$  are the scene radiance and transmitter irradiance, respectively. Note that the incoherent field approximation is valid as long as  $E[\rho(\mathbf{x})\rho^*(\tilde{\mathbf{x}})]$  has a correlation length within half of a wavelength of the carrier frequency of the transmitter of opportunity (see page 526 of [54]). Under the incoherent field approximation, we write  $E[J_T(\omega, \mathbf{x})J_T^*(\omega, \mathbf{x})] = R_T(\omega, \mathbf{x})$  where  $R_T$  denotes transmitter irradiance.

We now define the *phase-space radiance function* as

$$\begin{aligned} r(\mathbf{x}, \mathbf{v}) &= R_\rho(\mathbf{x})\delta(\mathbf{v} - \mathbf{v}_\mathbf{x}) \\ &\approx R_\rho(\mathbf{x})\varphi(\mathbf{v}, \mathbf{v}_\mathbf{x}), \end{aligned} \quad (9)$$

where  $\varphi(\mathbf{v}, \mathbf{v}_\mathbf{x})$  is a smooth, differentiable function of  $\mathbf{v}$  that approximates the Dirac delta function in the limit, such as a Gaussian or sinc function.

#### B. Forward Model for SAH/GMTI

Using (7)-(8), the expected value of the correlated received signal can be modeled as

$$\begin{aligned} d_{ij}(s, \tau) &= E[f_{ij}(s, \tau)] := \mathcal{F}[r](s, \tau) \\ &= \int e^{-i\omega[\tau - R_{ij}(\mathbf{x}, s)/c_0 - B_{ij}(\mathbf{x}, \mathbf{v}, s)/c_0]} \\ &\quad \times A_{ij}(\omega, s, \mathbf{x}, \mathbf{v})r(\mathbf{x}, \mathbf{v}) d\mathbf{v}d\mathbf{x}d\omega \end{aligned} \quad (10)$$

where

$$A_{ij}(\omega, s, \mathbf{x}, \mathbf{v}) = A_{R_{ij}}(\omega, s, \mathbf{x}, \mathbf{v}) \frac{R_T(\omega, \mathbf{x})}{(4\pi)^2 |\mathbf{x} + \mathbf{v}_x s - \mathbf{y}|^2} \quad (11)$$

$$A_{R_{ij}}(\omega, s, \mathbf{x}, \tilde{\mathbf{x}}, \mathbf{v}_x, \mathbf{v}_{\tilde{x}}) = \frac{J_{R_i}(\omega, \mathbf{x}, s) J_{R_j}^*(\omega, \tilde{\mathbf{x}}, s)}{(4\pi)^2 |\mathbf{x} + \mathbf{v}_x s - \gamma_i(s)| |\tilde{\mathbf{x}} + \mathbf{v}_{\tilde{x}} s - \gamma_j(s)|} \quad (12)$$

$$R_{ij}(\mathbf{x}, s) = |\mathbf{x} - \gamma_i(s)| - |\mathbf{x} - \gamma_j(s)| \quad (13)$$

$$B_{ij}(\mathbf{x}, \mathbf{v}, s) = [(\widehat{\mathbf{x} - \gamma_i(s)}) - (\widehat{\mathbf{x} - \gamma_j(s)})] \cdot \mathbf{v} s, \quad (14)$$

where  $\widehat{\mathbf{x}}$  is the unit vector in the direction of  $\mathbf{x}$ . We define

$$\mathbf{L}_{ij}(\mathbf{x}, s) = [(\widehat{\mathbf{x} - \gamma_i(s)}) - (\widehat{\mathbf{x} - \gamma_j(s)})] \quad (15)$$

as the *hitchhiker look direction*. In this model,  $R_{ij}$  is the *hitchhiker range* introduced in [6], and  $B_{ij}$  can be viewed as the displacement in the hitchhiker look direction due to the movement of the target at  $\mathbf{x}$ .

We assume that there is some  $m_A$  such that  $A_{ij}$  satisfies

$$\sup_{(\omega, s, \mathbf{x}) \in \mathcal{U}} |\partial_\omega^\alpha \partial_s^\beta \partial_{x_1}^{\rho_1} \partial_{x_2}^{\rho_2} A(\omega, s, \mathbf{x})| \leq C_A (1 + \omega^2)^{(m_A - |\alpha|)/2} \quad (16)$$

where  $\mathcal{U}$  is any compact subset of  $\mathbb{R} \times \mathbb{R} \times \mathbb{R}^2$  and  $C_A$  depends on  $\mathcal{U}$ ,  $\alpha$ ,  $\beta$ ,  $\rho_1$ , and  $\rho_2$ . Under (16), the forward operator  $\mathcal{F}$  is defined as a Fourier Integral Operator (FIO) [55], [56]. The phase term of  $\mathcal{F}$  is given by

$$\phi_{ij}(\omega, \mathbf{x}, \mathbf{v}, \tau, s) = \omega[\tau - R_{ij}(\mathbf{x}, s)/c_0 - B_{ij}(\mathbf{x}, \mathbf{v}, s)/c_0] \quad (17)$$

and its amplitude term is  $A_{ij}$  as defined in (11).

We now pose the passive synthetic aperture imaging of moving targets as the inversion of the forward map  $\mathcal{F}$ .

### C. Critical Points of the Forward Model

An FIO can be viewed as a generalized Radon transform that projects the weighted or filtered version of an input function onto some smooth manifolds such as circles, ellipsoids etc. The weighting or filtering is defined by the amplitude term and the smooth manifolds are defined by the phase function of the FIO. If the amplitude function is identically equal to 1, then the FIO simply projects the input function onto the manifolds defined by its phase term. To understand the underlying geometry, the nature of the data  $d_{ij}$  that will be used for inversion, and to develop an inverse map for  $\mathcal{F}$ , we study the geometry of these curved manifolds.

The main contributions to  $d_{ij}$  come from the projection of the phase-space radiance function onto the curved manifolds which are given by the critical set  $\{(\mathbf{x}, \mathbf{v}) \in \mathbb{R}^2 \times \mathbb{R}^2 : \partial_\omega \phi = 0, (\mathbf{x}, \mathbf{v}) \in \text{supp}(A_{ij})\}$  of the phase  $\phi$  [55], [56]. We denote these four-dimensional surfaces defined in position and velocity spaces by

$$H_{ij}(s, \tau) = \{(\mathbf{x}, \mathbf{v}) \in \mathbb{R}^2 \times \mathbb{R}^2 : R_{ij}(\mathbf{x}, s) + B_{ij}(\mathbf{x}, \mathbf{v}, s) = \tau c_0\} \quad (18)$$

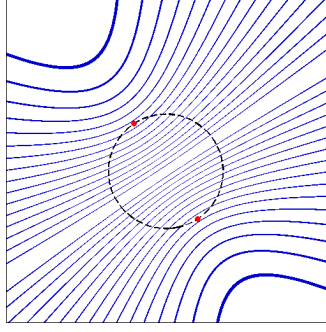


Fig. 1. Position-space iso-range contours for a stationary target. In this case the contours in 4D space are hyperboloids, and when intersected with a flat topography form the hyperbolas shown here.

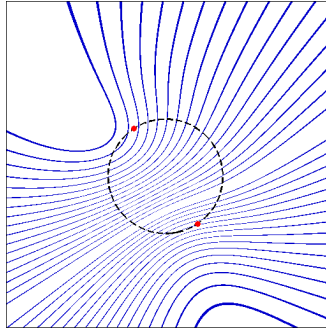


Fig. 2. Position-space iso-range contours for a moving target with velocity (50,100) on a flat topography and two receivers cross-correlating their data. With zero velocity, these curves would be hyperbolas, but the moving target warps these contours.

and refer to them as *hitchhiker moving target iso-range surfaces*. In order to visualize this four-dimensional manifold we consider the following two cross sections for constant velocity and constant position:

$$H_{ij,\mathbf{v}_0}(s, \tau) = \{\mathbf{x} \in \mathbb{R}^2 : R_{ij}(\mathbf{x}, s) + B_{ij}(\mathbf{x}, \mathbf{v}_0, s) = \tau c_0, (\mathbf{x}, \mathbf{v}_0) \in \text{supp}(A_{ij})\} \quad (19)$$

$$H_{ij,\mathbf{x}_0}(s, \tau) = \{\mathbf{v} \in \mathbb{R}^2 : R_{ij}(\mathbf{x}_0, s) + B_{ij}(\mathbf{x}_0, \mathbf{v}, s) = \tau c_0, (\mathbf{x}_0, \mathbf{v}) \in \text{supp}(A_{ij})\}. \quad (20)$$

We refer to  $H_{ij,\mathbf{v}_0}$  as the *position-space hitchhiker iso-range curve* and  $H_{ij,\mathbf{x}_0}$  as the *velocity-space hitchhiker iso-range curve*. Figures 1 and 2 show examples of position-space iso-range contours for a flat topography ( $\psi(\mathbf{x}) = 0$ ). Figure 1 shows position-space curves with an assumption of zero velocity for the moving target. The manifolds in 4D space are hyperboloids with the two receivers as foci, and they form hyperbolas when intersected with the ground. A non-zero velocity warps these contours, as shown in Figure 2.

#### IV. IMAGE FORMATION

The goal for reconstruction is to form an image that is simultaneously focused in both position and velocity spaces. A logical choice would be to backproject the data onto the four-dimensional hitchhiker moving target iso-range surfaces described in the previous section. However, since the data in hand is only two-dimensional, we may not be able to reconstruct the image so that the underlying point spread function (PSF) is approximately a Dirac delta function in both the position and velocity spaces.

To reconstruct a position (radiance) image of the scene, we assume a fixed, hypothesized velocity  $\mathbf{v}_h$  for the scene and then backproject onto the two-dimensional position-space iso-range cross section for  $\mathbf{v}_h$ . We refer to this position image as the  $\mathbf{v}_h$ -radiance image. We show in the point spread function analysis section that whenever  $\mathbf{v}_h$  is equal to the true velocity  $\mathbf{v}_x$  of the scatterer at  $\mathbf{x}$ , backprojecting onto the position-space iso-range cross section places the reconstructed scatterer at the correct location. We next design the filter so that the PSF of the imaging operator is approximately a Dirac delta function. We perform this process for a range of hypothesized velocities, yielding a stack of these  $\mathbf{v}_h$ -radiance images. By measuring the entropy of each image, we can determine the degree of smearing of the scatterers, and simultaneously the accuracy of the hypothesized velocities. We search the stack of images for the one with the lowest entropy along with their corresponding velocity estimates for each target.

##### A. Filtered Backprojection Operator

For a given velocity  $\mathbf{v}_h$  and a given pair of receivers, we define the filtered backprojection operator as

$$\begin{aligned} \mathcal{K}[d_{ij}](\mathbf{x}') &= \hat{r}_{ij}^{\mathbf{v}_h}(\mathbf{x}') \\ &= \int e^{i\omega[\tau - R_{ij}(\mathbf{x}', s)/c_0 - B_{ij}(\mathbf{x}', \mathbf{v}_h, s)/c_0]} d_{ij}(s, \tau) \\ &\quad \times Q_{ij}^{\mathbf{v}_h}(\omega, s, \mathbf{x}') d\omega ds d\tau, \end{aligned} \quad (21)$$

where  $Q_{ij}^{\mathbf{v}_h}(\omega, s, \mathbf{x}')$  is the filter to be determined later.

Under the assumption that  $Q_{ij}^{\mathbf{v}_h}$  satisfies a similar condition to (16),  $\mathcal{K}$  becomes an FIO. Note that  $\mathbf{v}_h$  is simply a fixed parameter, not an argument of  $\mathcal{K}$ .

Our reconstructed image is the sum of all pairs of images  $\hat{r}_{ij}^{\mathbf{v}_h}$ :

$$\hat{r}^{\mathbf{v}_h}(\mathbf{x}') = \sum_{i,j} \hat{r}_{ij}^{\mathbf{v}_h}(\mathbf{x}') \quad i \neq j, \quad i, j = 1, \dots, N, \quad (22)$$

Note that the assumption of linear target motion can be violated for sufficiently long apertures or CPI. However, use of multiple pairs of receivers can extend the effective aperture length without extending the CPI, compensating for potential loss of resolution due to short CPI.

### B. Point Spread Function of the Imaging Operator

By substituting (10) into (22) and performing the  $d\tau$  integration by setting  $\omega = \omega'$ , we obtain

$$\begin{aligned} \hat{r}^{\mathbf{v}_h}(\mathbf{x}') &= \sum_{i,j} \int e^{i\omega[R_{ij}(\mathbf{x}',s)/c_0 + B_{ij}(\mathbf{x}',\mathbf{v}_h,s)/c_0]} \\ &\quad \times e^{-i\omega[R_{ij}(\mathbf{x},s)/c_0 + B_{ij}(\mathbf{x},\mathbf{v},s)/c_0]} \\ &\quad \times A_{ij}(\omega, s, \mathbf{x}, \mathbf{v}) Q_{ij}^{\mathbf{v}_h}(\omega, s, \mathbf{x}') \\ &\quad \times r(\mathbf{x}, \mathbf{v}) d\mathbf{x}d\mathbf{v}d\omega ds \\ &= \mathcal{KF}[r](\mathbf{x}'). \end{aligned} \quad (23)$$

Our image fidelity operator is in the form

$$\hat{r}^{\mathbf{v}_h}(\mathbf{x}') = \sum_{i,j} \int L_{ij}^{(\mathbf{v},\mathbf{v}_h)}(\mathbf{x}, \mathbf{x}') r(\mathbf{x}, \mathbf{v}) d\mathbf{x}d\mathbf{v} \quad (24)$$

$$\begin{aligned} L_{ij}^{(\mathbf{v},\mathbf{v}_h)}(\mathbf{x}, \mathbf{x}') &= \\ &\int e^{i\omega[R_{ij}(\mathbf{x}',s)/c_0 + B_{ij}(\mathbf{x}',\mathbf{v}_h,s)/c_0 - R_{ij}(\mathbf{x},s)/c_0 - B_{ij}(\mathbf{x},\mathbf{v},s)/c_0]} \\ &\quad \times A_{ij}(\omega, s, \mathbf{x}, \mathbf{v}) Q_{ij}^{\mathbf{v}_h}(\omega, s, \mathbf{x}') d\omega ds, \end{aligned} \quad (25)$$

where  $L_{ij}^{(\mathbf{v},\mathbf{v}_h)}(\mathbf{x}, \mathbf{x}')$  is the point spread function of the imaging operator.

### C. Analysis of the Point Spread Function

We analyze the PSF of the imaging operator  $\mathcal{K}$  to understand the geometric fidelity of the reconstructed  $\mathbf{v}_h$ -radiance images. In particular, we want to determine if a visible edge or a point scatterer in the scene is located at the right position and orientation in the image. To address this question, we use microlocal analysis.

Let

$$\begin{aligned} \Phi_{ij}^{(\mathbf{v},\mathbf{v}_h)}(\omega, s, \mathbf{x}', \mathbf{x}) &= \omega[R_{ij}(\mathbf{x}',s)/c_0 + B_{ij}(\mathbf{x}',\mathbf{v}_h,s)/c_0 \\ &\quad - R_{ij}(\mathbf{x},s)/c_0 - B_{ij}(\mathbf{x},\mathbf{v},s)/c_0] \end{aligned} \quad (26)$$

denote the phase of the image fidelity operator  $\mathcal{KF}$ . By the Hörmander-Sato theorem [55], [56], we conclude that the imaging operator  $\mathcal{K}$  reconstructs the visible edges (scatters) located at  $\mathbf{x}$  with velocity  $\mathbf{v}$  to location  $\mathbf{x}'$  with velocity  $\mathbf{v}_h$  in the image satisfying the following conditions:

$$\partial_\omega \Phi_{ij}^{(\mathbf{v},\mathbf{v}_h)}(\omega, s, \mathbf{x}', \mathbf{x}) = 0 \quad (27)$$

$$\partial_s \Phi_{ij}^{(\mathbf{v},\mathbf{v}_h)}(\omega, s, \mathbf{x}', \mathbf{x}) = 0. \quad (28)$$

Alternatively, at image location  $\mathbf{x}'$ ,  $\mathcal{K}$  reconstructs the visible edges of the scene at locations  $\mathbf{x}$  that satisfy the conditions in (27) and (28). These conditions yield the surfaces

$$R_{ij}(\mathbf{x}', s) + B_{ij}(\mathbf{x}', \mathbf{v}_h, s) = R_{ij}(\mathbf{x}, s) + B_{ij}(\mathbf{x}, \mathbf{v}, s) \quad (29)$$

$$\dot{R}_{ij}(\mathbf{x}', s) + \dot{B}_{ij}(\mathbf{x}', \mathbf{v}_h, s) = \dot{R}_{ij}(\mathbf{x}, s) + \dot{B}_{ij}(\mathbf{x}, \mathbf{v}, s), \quad (30)$$

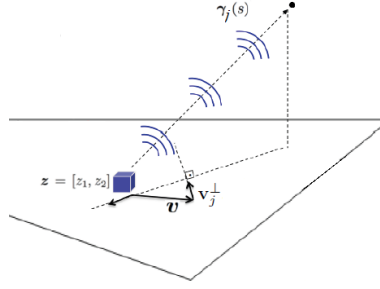


Fig. 3. Geometry of the  $\mathbf{v}_j^\perp$  vector, which is the target's velocity projected onto the direction perpendicular to the antenna look direction.

where  $\mathbf{x} = [\mathbf{x}, \psi(\mathbf{x})]$ ,  $\mathbf{v} = [\mathbf{v}, \nabla_{\mathbf{x}}\psi(\mathbf{x}) \cdot \mathbf{v}]$ ,  $[\mathbf{x}, \mathbf{v}, \mathbf{x}', \mathbf{v}_h] \in \text{supp}(A_{ij}Q_{ij}^{\mathbf{v}_h})$ ; and  $\dot{R}_{ij}$  and  $\dot{B}_{ij}$  are the derivatives with respect to  $s$  of  $R_{ij}$  and  $B_{ij}$ , respectively.

For a fixed  $\mathbf{x}'$  and  $\mathbf{v}_h$ , (29) describes hitchhiker iso-range contours for moving targets. These contours satisfy the equation

$$R_{ij}(\mathbf{x}, s) + B_{ij}(\mathbf{x}, \mathbf{v}, s) = C_R \quad (31)$$

$$\begin{aligned} & |\mathbf{x} - \widehat{\gamma}_i(s)| - |\mathbf{x} - \widehat{\gamma}_j(s)| + [(\widehat{\mathbf{x}} - \widehat{\gamma}_i(s)) - (\widehat{\mathbf{x}} - \widehat{\gamma}_j(s))] \cdot \mathbf{v}s \\ & = C_R, \quad (\mathbf{x}, \mathbf{v}) \in \text{supp}(A_{ij}), \end{aligned} \quad (32)$$

where  $C_R$  is a constant.

Similarly, for a fixed  $\mathbf{x}'$  and  $\mathbf{v}_h$ , (30) describes a set in  $(\mathbf{x}, \mathbf{v})$  satisfying

$$\partial_s R_{ij}(\mathbf{x}, s) + \partial_s B_{ij}(\mathbf{x}, \mathbf{v}, s) = C_D \quad (33)$$

$$\begin{aligned} & (\widehat{\mathbf{x}} - \widehat{\gamma}_i(s)) \cdot (\mathbf{v} - \dot{\gamma}_i(s)) - (\widehat{\mathbf{x}} - \widehat{\gamma}_j(s)) \cdot (\mathbf{v} - \dot{\gamma}_j(s)) \\ & - \frac{\dot{\gamma}_i(s)s}{|\mathbf{x} - \widehat{\gamma}_i(s)|} \cdot \mathbf{v}_i^\perp + \frac{\dot{\gamma}_j(s)s}{|\mathbf{x} - \widehat{\gamma}_j(s)|} \cdot \mathbf{v}_j^\perp = C_D \\ & (\mathbf{x}, \mathbf{v}) \in \text{supp}(A_{ij}), \end{aligned} \quad (34)$$

where  $C_D$  is a constant and

$$\mathbf{v}_i^\perp = \mathbf{v} - (\widehat{\mathbf{x}} - \widehat{\gamma}_i(s))[(\widehat{\mathbf{x}} - \widehat{\gamma}_i(s)) \cdot \mathbf{v}] \quad (35)$$

$$\mathbf{v}_j^\perp = \mathbf{v} - (\widehat{\mathbf{x}} - \widehat{\gamma}_j(s))[(\widehat{\mathbf{x}} - \widehat{\gamma}_j(s)) \cdot \mathbf{v}]. \quad (36)$$

The  $\mathbf{v}_i^\perp$  and  $\mathbf{v}_j^\perp$  vectors are the three-dimensional target velocities projected onto the direction perpendicular to the look directions of the two receivers. The equation describing the iso-Doppler contours is derived in Appendix A. Figure 3 shows the geometry of this vector.

We refer to the set  $(\mathbf{x}, \mathbf{v})$  satisfying (34) as the *hitchhiker iso-Doppler contours for moving targets*. We define the cross-sections of this set for fixed velocity as the position-space hitchhiker iso-Doppler contours, and for fixed position as the velocity-space hitchhiker iso-Doppler contours.

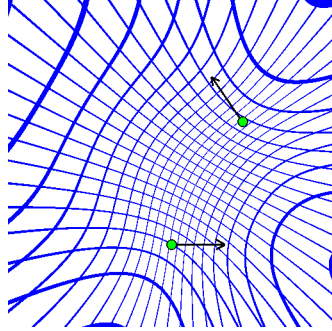


Fig. 4. Intersection of the position space iso-range and iso-Doppler curves for flat topography. The green circles are the two receiving antennas, with their velocity vectors shown as arrows.

The position space iso-range contours in (32), as described in Section III-C, are the intersections of warped hyperboloids with the ground topography.

The imaging operator reconstructs visible edges at the intersection of hitchhiker iso-range and iso-Doppler contours. Since one of the solutions of (27) and (28) is  $\mathbf{x} = \mathbf{x}'$  for  $\mathbf{v}_x = \mathbf{v}_h$ , we conclude that the imaging operator puts the visible edges at the right location in the image. However, (27) and (28) may have additional solutions, resulting in artifacts in the reconstructed image. Some of these artifacts may be prevented by choosing an appropriate support for  $A_{ij}$  (illumination pattern) and appropriate flight trajectories for receivers. Figure 4 shows the intersection of the position space iso-range and iso-Doppler contours for particular antenna locations and antenna velocities indicated by solid dots and arrows. The figure suggests that in order to eliminate artifacts and ambiguities, the two receivers have to look at the same side of the scene with respect to the conjugate axis of the warped hyperbolas.

#### D. Determination of the FBP Filter

In the previous subsection, we showed that the imaging operator can reconstruct a position image of a scatterer at the correct location and orientation irrespective of the choice of the filter  $Q_{ij}$ , as long as the hypothesized velocity of a scatterer is equal to its true velocity. In this section, we derive the filter such that the strength or contrast of the scatterer is also determined correctly. To do so, we choose the filter  $Q_{ij}$  such that the PSF of the imaging operator for each pair of receivers is approximately the Dirac delta function under the assumption that the hypothesized velocity  $\mathbf{v}_h$  equals the true velocity  $\mathbf{v}_x$ :

$$\begin{aligned} L_{ij}^{(\mathbf{v}_h, \mathbf{v}_h)}(\mathbf{x}, \mathbf{x}') &\approx \delta(\mathbf{x} - \mathbf{x}') \\ &= \int e^{i(\mathbf{x} - \mathbf{x}') \cdot \boldsymbol{\xi}} d\boldsymbol{\xi}. \end{aligned} \quad (37)$$

To obtain the desired PSF given in (37) we make a Taylor series approximation of the phase around the point

$\mathbf{x} = \mathbf{x}'$ :

$$\begin{aligned} \Phi_{ij}^{(\mathbf{v}_h, \mathbf{v}_h)}(\omega, s, \mathbf{x}', \mathbf{x}) &\approx \\ &(\mathbf{x} - \mathbf{x}') \frac{\omega}{c_0} \nabla_{\mathbf{x}} [-R_{ij}(\mathbf{x}, s) - B_{ij}(\mathbf{x}, \mathbf{v}_h, s)]|_{\mathbf{x}=\mathbf{x}'}. \end{aligned} \quad (38)$$

Let

$$\Xi_{ij}(s, \mathbf{x}', \mathbf{v}_h) = \nabla_{\mathbf{x}} [-R_{ij}(\mathbf{x}, s) - B_{ij}(\mathbf{x}, \mathbf{v}_h, s)]|_{\mathbf{x}=\mathbf{x}'} \quad (39)$$

and

$$\xi_{ij} = \frac{\omega}{c_0} \Xi_{ij}(s, \mathbf{x}', \mathbf{v}_h). \quad (40)$$

We now make the change of variables

$$(\omega, s) \rightarrow \xi_{ij} = \frac{\omega}{c_0} \Xi_{ij}(s, \mathbf{x}', \mathbf{v}_h) \quad (41)$$

in the PSF to obtain

$$\begin{aligned} L_{ij}^{(\mathbf{v}_h, \mathbf{v}_h)}(\mathbf{x}, \mathbf{x}') &= \int_{\Omega_{ij}} e^{i(\mathbf{x}-\mathbf{x}') \cdot \xi_{ij}} A_{ij}(\xi_{ij}, \mathbf{x}', \mathbf{v}_h) \\ &Q_{ij}^{v_h}(\xi_{ij}, \mathbf{x}') \eta(\xi_{ij}, \mathbf{x}', \mathbf{v}_h) d\xi_{ij} \end{aligned} \quad (42)$$

where  $\eta$  is the determinant of the Jacobian that comes from the change of variables in (41)

$$\eta(\xi_{ij}, \mathbf{x}', \mathbf{v}_h) = \left| \frac{\partial(\omega, s)}{\partial \xi_{ij}} \right|, \quad (43)$$

and

$$\Omega_{ij} = \{\xi_{ij} : \xi_{ij} = \frac{\omega}{c_0} \Xi_{ij}(s, \mathbf{x}', \mathbf{v}_h), A_{ij}(\xi_{ij}, \mathbf{x}', \mathbf{v}_h) \neq 0\}. \quad (44)$$

In (42), for notational convenience, we redefine

$$A_{ij}(\xi_{ij}, \mathbf{x}', \mathbf{v}_h) = A_{ij}(\omega(\xi_{ij}), s(\xi_{ij}), \mathbf{x}', \mathbf{v}_h) \quad (45)$$

$$Q_{ij}^{v_h}(\xi_{ij}, \mathbf{x}') = Q_{ij}^{v_h}(\omega(\xi_{ij}), s(\xi_{ij}), \mathbf{x}'). \quad (46)$$

We refer to the set  $\Omega_{ij}$  as the data collection manifold at  $\mathbf{x}'$ . Clearly, the vector  $\xi_{ij}$  can be interpreted as the Fourier vector that contributes to the reconstruction of a pixel at  $\mathbf{x}'$ . The set  $\Omega_{ij}$  and the vector  $\xi_{ij}$  describes many of the properties of the reconstructed image as will be discussed in Part 2.

Since we desire our filter to make the PSF an approximate Dirac delta function, the optimal filter becomes

$$\begin{aligned} Q_{ij}^{v_h}(\xi_{ij}, \mathbf{x}', \mathbf{v}_h) &= \frac{\chi_{\Omega} A_{ij}^*(\xi_{ij}, \mathbf{x}', \mathbf{v}_h)}{\eta(\xi_{ij}, \mathbf{x}', \mathbf{v}_h) |A_{ij}(\xi_{ij}, \mathbf{x}', \mathbf{v}_h)|^2} \\ &= \frac{\chi_{\Omega} A_{ij}^*(\xi_{ij}, \mathbf{x}', \mathbf{v}_h) |\omega|}{|A_{ij}(\xi_{ij}, \mathbf{x}', \mathbf{v}_h)|^2 c_0^2} \\ &\quad \times |\Xi_{ij,1} \dot{\Xi}_{ij,2} - \Xi_{ij,2} \dot{\Xi}_{ij,1}|, \end{aligned} \quad (47)$$

where  $\chi_{\Omega}$  is a smooth cut-off function to prevent division by zero and  $\Xi_{ij} = [\Xi_{ij,1}, \Xi_{ij,2}]$ .

The direction of the  $\xi_{ij}$  vector is defined by the vector  $\Xi_{ij}$  which is given by

$$\begin{aligned} \Xi_{ij}(s, \mathbf{x}', \mathbf{v}_h) &= -D\psi(\mathbf{x}') \cdot [(\widehat{\mathbf{x}' - \gamma_i(s)}) - (\widehat{\mathbf{x}' - \gamma_j(s)})] \\ &\quad - \frac{D\psi(\mathbf{x}') \cdot \mathbf{v}_{h,i}^\perp s + \partial_{\mathbf{x}'}^2 \psi(\mathbf{x}') \cdot \mathbf{v}_h(\psi(\mathbf{x}') - \gamma_i^3(s))s}{|\mathbf{x}' - \gamma_i(s)|} \\ &\quad + \frac{D\psi(\mathbf{x}') \cdot \mathbf{v}_{h,j}^\perp s + \partial_{\mathbf{x}'}^2 \psi(\mathbf{x}') \cdot \mathbf{v}_h(\psi(\mathbf{x}') - \gamma_j^3(s))s}{|\mathbf{x}' - \gamma_j(s)|}, \end{aligned} \quad (48)$$

where

$$D\psi(\mathbf{x}') = \begin{bmatrix} 1 & 0 & \partial\psi(\mathbf{x}')/\partial x'_1 \\ 0 & 1 & \partial\psi(\mathbf{x}')/\partial x'_2 \end{bmatrix} \quad (49)$$

$$\partial_{\mathbf{x}'}^2 = \begin{bmatrix} \partial^2/\partial x_1'^2 & \partial^2/\partial x_1'x_2' \\ \partial^2/\partial x_2'x_1' & \partial^2/\partial x_2'^2 \end{bmatrix}, \quad (50)$$

and the matrix  $D\psi(\mathbf{x}')$  projects a 3D vector onto the tangent plane of the ground topography, and the  $\partial_{\mathbf{x}'}^2$  matrix is the Hessian operator. The derivation for the  $\Xi_{ij}$  vector can be found in Appendix B.

In the case of flat topography ( $\psi(\mathbf{x}') = 0$ ), (48) reduces to

$$\Xi_{ij}(s, \mathbf{x}', \mathbf{v}_h) = \Xi_{ij,1}(s, \mathbf{x}', \mathbf{v}_h) + \Xi_{ij,2}(s, \mathbf{x}', \mathbf{v}_h) \quad (51)$$

where

$$\Xi_{ij,1}(s, \mathbf{x}', \mathbf{v}_h) = D\psi(\mathbf{x}') \cdot [(\widehat{\mathbf{x}' - \gamma_j(s)}) - (\widehat{\mathbf{x}' - \gamma_i(s)})] \quad (52)$$

$$\Xi_{ij,2}(s, \mathbf{x}', \mathbf{v}_h) = \frac{D\psi(\mathbf{x}') \cdot \mathbf{v}_{h,j}^\perp s}{|\mathbf{x}' - \gamma_j(s)|} - \frac{D\psi(\mathbf{x}') \cdot \mathbf{v}_{h,i}^\perp s}{|\mathbf{x}' - \gamma_i(s)|}. \quad (53)$$

The first component is a function of the antenna locations and imaging geometry. This term remains the same as in the stationary case derived in our work [6]. The second term is due to the movement of the targets.

The filter  $\Xi_{ij}(s, \mathbf{x}', \mathbf{v}_h)$  depends on  $A_{ij}$  and therefore both  $R_T(\omega, \mathbf{x})$  and the transmitter-related geometric spreading term. When this information is unavailable, we can assume a uniform prior on  $R_T$ , corresponding to a white noise model for the ambient electromagnetic signal, and we can approximate the geometric spreading up to the radius of the imaging region of interest assuming the transmitter lies outside of this region. Since we are performing the imaging coherently, i.e. by matching the phase of the forward operator with the imaging operator, which does not include any of the terms above, the Jacobian resulting from the change of variables in the phase (41) plays a more significant role in obtaining the correct strengths of the scatterers than the other terms involved in the filter. In addition, the scatterers will also be correctly positioned in the reconstruction image, since this is a function only of the phase matching procedure.

### E. Velocity Estimation

To estimate the velocities of targets, we reconstruct a series of radiance images, each using a fixed hypothesized velocity for a range of velocities. Images that are reconstructed with an incorrect hypothesized velocity have smeared

targets, while the image with the correct velocity will have a focused target. We present an analysis of the degree and nature of smearing in reconstructed images due to incorrect velocity in Part 2 of this sequence of papers.

There are a variety of metrics to measure the degree of focus in SAR images [44]–[51]. See [50] for a review of these metrics. We chose Shannon entropy as a measure of focus for each reconstructed image. Entropy provides distinct benefits for SAR, which includes being a sensitive measure of image focus quality, having a smooth dependence on autofocus parameters, and requiring no specific target or clutter model [48]. In general, one may choose to compute the image entropy over an energy-weighted version of the image as

$$g^{v_h}(\mathbf{x}') = w(\mathbf{x}')\hat{r}^{v_h}(\mathbf{x}'), \quad (54)$$

where  $w(\mathbf{x}')$  is a two-dimensional weighting function as described in [49]. To use the original image,  $w(\mathbf{x}')$  can simply be set to 1 for all  $\mathbf{x}'$ . To use a patch of the original image,  $w(\mathbf{x}')$  can be set to 1 on the patch and zero outside. For various other choices of “energy” weighting, see [50].

We measure the degree of focus of each image, and we presume the images with the highest focus yield the correct velocity estimates. For a given radiance image reconstructed using the hypothesized velocity  $v_h$ , its entropy is defined as

$$\text{En}(v_h) = - \int p(g^{v_h}(\mathbf{x}')) \log[p(g^{v_h}(\mathbf{x}'))] d\mathbf{x}', \quad (55)$$

where  $p$  is the probability density function or the normalized histogram of the image in the discrete case. As the error between true and hypothesized velocity of moving targets increases, the smearing artifacts increase, resulting in higher computed entropy values. Thus, the local minima of  $\text{En}$  correspond to the estimated target velocities.

If the number of moving targets in the scene is known prior to velocity estimation, then this number of minimum entropy images can simply be chosen from the image stack. If this quantity is unknown, however, then a criterion, such as constant false alarm rate, can be used to determine the number of moving targets in the scene [57]. The images reconstructed with the hypothesized velocities corresponding to the lowest entropy values then each display a focused (or nearly focused, considering the effects of noise and clutter) target moving with that particular velocity.

## V. COMPUTATIONAL COMPLEXITY ANALYSIS

This section describes the algorithmic implementation of our method and analyze its computational complexity.

Our image reconstruction formula for a hypothesized velocity is presented in (22). After performing the  $d\tau$  integration, the formula becomes

$$\begin{aligned} \hat{r}^{v_h}(\mathbf{x}') &= \sum_{i,j} \int e^{-i\omega[-R_{ij}(\mathbf{x}',s)/c_0 - B_{ij}(\mathbf{x}',v_h,s)/c_0]} \\ &\quad \times D_{ij}(s,\omega) Q_{ij}^{v_h}(\omega,s,\mathbf{x}') d\omega ds \end{aligned} \quad (56)$$

where  $D_{ij}(s,\omega)$  is the Fourier transform of  $d_{ij}(s,\tau)$  in the  $\tau$  direction. Furthermore, the filter  $Q_{ij}$  can be decomposed as

$$Q_{ij}^{v_h}(\omega,s,\mathbf{x}') = Q_{ij}^{v_h,1}(s,\mathbf{x}') Q_{ij}^{v_h,2}(\omega,s,\mathbf{x}') |\omega| \quad (57)$$

where

$$Q_{ij}^{v_h,1}(s, \mathbf{x}') = |\Xi_{ij,1}\dot{\Xi}_{ij,2} - \Xi_{ij,2}\dot{\Xi}_{ij,1}| \quad (58)$$

$$Q_{ij}^{v_h,2}(\omega, s, \mathbf{x}') = \frac{\chi_{\Omega} A_{ij}^*(\omega, s, \mathbf{x}', \mathbf{v}_h)}{|A_{ij}(\omega, s, \mathbf{x}', \mathbf{v}_h)|^2 c_0^2}. \quad (59)$$

Here, the  $|\omega|$  factor is the well-known ramp filter from the tomography literature, the  $Q_{ij}^{v_h,1}$  filter compensates for the change of variables, and the  $Q_{ij}^{v_h,2}$  filter reverses the effects of the amplitude factor, which includes the beam pattern, waveform, and geometric spreading factors.

Assuming  $\mathcal{O}(N)$  samples in both fast-time and slow-time and a scene sampled at  $\mathcal{O}(N \times N)$  points, the image reconstruction procedure for a hypothesized velocity  $\mathbf{v}_h$  can be implemented as follows:

- 1) *Correlating each pair of receiver data in fast-time:* The received signals for each pair of antennas are cross-correlated using (6) at each slow-time  $s$ . Therefore, for all  $s$ , the computational complexity of this step is  $\mathcal{O}(N^2)$ .
- 2) *Computing the Fourier transform in fast-time:* For each  $s$  the Fourier transform of  $d_{ij}(s, \tau)$  can be computed in  $\mathcal{O}(N \log N)$  computations, so for all  $s$ , this step has a computational complexity of  $\mathcal{O}(N^2 \log N)$ . Note that if FFT-based cross-correlation is used in Step 1, these first two steps can be combined.
- 3) *Ramp filtering:* Let

$$\tilde{D}_{ij}(s, \omega) = |\omega| D_{ij}(s, \omega). \quad (60)$$

For each  $s$ , this filtering can be computed in  $\mathcal{O}(N)$  computations, making the computational complexity of this step  $\mathcal{O}(N^2)$ .

- 4) *Filtering with  $Q_{ij}^{v_h,2}$ :* Let

$$\tilde{D}_{ij, Q_{ij}^{v_h,2}}(s, \omega, \mathbf{x}') = \tilde{D}_{ij}(s, \omega) Q_{ij}^{v_h,2}(\omega, s, \mathbf{x}'). \quad (61)$$

For each  $s$  and  $\mathbf{x}'$ , this filtering can be performed in  $\mathcal{O}(N)$  computations, so the computational complexity of this step is  $\mathcal{O}(N^4)$  in general. If  $Q_{ij}^{v_h,2}$  is independent of  $\mathbf{x}'$  however, this step reduces to  $\mathcal{O}(N^2)$ .

- 5) *Backprojection:* Let

$$\hat{r}_{ij, Q_{ij}^{v_h,2}}(\mathbf{x}', s) = \int e^{-i\omega[-R_{ij}(\mathbf{x}', s)/c_0 - B_{ij}(\mathbf{x}', \mathbf{v}_h, s)/c_0]} \quad (62)$$

$$\times \tilde{D}_{ij, Q_{ij}^{v_h,2}}(s, \omega, \mathbf{x}') d\omega. \quad (63)$$

For each  $s$  and  $\mathbf{x}'$ , (63) can be computed in  $\mathcal{O}(N)$  computations. Thus, for all  $s$  and  $\mathbf{x}'$ , the computational complexity of this step is  $\mathcal{O}(N^4)$ .

- 6) *Partial image formation:* We form the partial image using

$$\hat{r}_{ij}^{v_h}(\mathbf{x}') = \int Q_{ij}^{v_h,1}(s, \mathbf{x}', \mathbf{v}_h) \hat{r}_{ij, Q_{ij}^{v_h,2}}(\mathbf{x}', s) ds. \quad (64)$$

For each point  $\mathbf{x}'$  this integral can be computed in  $\mathcal{O}(N)$ , so the computational complexity of this step is  $\mathcal{O}(N^3)$ .

7) *Complete image formation:* We form our final image via

$$\hat{r}^{v_h}(\mathbf{x}') = \sum_{i,j} \hat{r}_{ij}^{v_h}(\mathbf{x}'). \quad (65)$$

Assuming the number of receiver pairs is much less than  $N$ , the overall computational complexity of complete image formation is equal to the highest computational complexity of each of the steps. Therefore, the overall complexity for image formation is  $\mathcal{O}(N^4)$ . Note that for the case of a large number of receiver pairs, the complexity of this step will scale linearly with the number of receiver pairs.

8) *Entropy calculation:* Compute  $\text{En}(v_h)$  by calculating the entropy for each image in the stack with the formula

$$\text{En}(v_h) = - \sum_{\mathbf{x}'} p(\hat{r}^{v_h}(\mathbf{x}')) \log[p(\hat{r}^{v_h}(\mathbf{x}'))]. \quad (66)$$

The computational complexity of the entropy calculation will be  $\mathcal{O}(N^2)$  for each of the histogram calculation, logarithm computation, and summation, yielding a complexity of  $\mathcal{O}(N^2)$  for the overall step.

The computational complexity of the full image formation procedure will be that of the step with the highest complexity, which in the above form is dominated by the filtering and backprojection steps of  $\mathcal{O}(N^4)$ . The backprojection method described above is a Fourier-based technique. This can instead be implemented efficiently by using fast backprojection algorithms [58]–[60] or fast Fourier integral operator computation methods [52], [61], [62]. For example, with the fast Fourier integral operator computation method presented in [52], the filtered backprojection step can be performed with a computational complexity of  $\mathcal{O}(N^2 \log N)$ .

This image formation processes is repeated for each hypothesized velocity, and the images with the lowest entropy values are then chosen. Assuming  $\mathcal{O}(M)$  hypothesized velocities, the full image reconstruction and velocity estimation procedure will have a computational complexity of  $\mathcal{O}(MN^4)$ , or of  $\mathcal{O}(MN^2 \log N)$  if the fast Fourier integral operator algorithm mentioned above is used. However, if we assume that  $M \ll N$ , the full image reconstruction and velocity computational complexity reduces to the complexity of the single image formation procedure.

## VI. NUMERICAL SIMULATIONS

### A. Simulation Setup

This section describes the numerical simulations that were performed in order to demonstrate the algorithm and its performance. In Part 2 of this paper we perform simulations to demonstrate properties relating to resolution and position error. We simulate a moving scene of size  $512 \times 512$  meters that is discretized into  $128 \times 128$  pixels, so that each pixel represents 4 square meters. The receiving antennas move in a circular aperture at a tangential velocity of 261 m/s. The circular aperture has a radius of 1.5 km, an altitude of 1 km, and is discretized into 2048 equally spaced samples.

Note that the assumption of targets having linear motion while the antennas are traversing a circular aperture may not be valid. However, this particular configuration was chosen so that velocity estimation-related effects can be deconvolved from potential limited-aperture artifacts.

The transmitter is a stationary tower located outside the circular flight trajectory at a distance of about 2.1 km from the center of the scene. The transmitter is using a rectangular pulse with an effective bandwidth of about 8 MHz. This is similar to the higher bandwidths used by sources of opportunity such as DVB-T and WiMax [1]. A graphical illustration of this setup is shown in Figure 5.

The velocities of the targets were varied to demonstrate the performance of the algorithm. The moving targets were simulated with speeds in the range of about 10 to 30 m/s, which is aligned with a range of normal vehicle speeds. For the hypothesized velocity, the speeds of the moving targets were assumed to be between 0 and 45 m/s. Therefore, the two-dimensional hypothesized velocity was varied from -45 to 45 m/s in each dimension with a step size of 2.25 m/s.

The data was generated by stepping through each slow-time and summing the signals scattered from each moving target in the scene. The velocity estimation and image reconstruction steps were then performed as described in Section V. Note that the image reconstruction and velocity estimation procedure is based on the forward model, which is only an approximation to the method by which the data is collected. Additionally, as described in Section IV-D, we used an uninformative prior for the second-order statistics of the antenna beam patterns as well as constant geometric spreading factors in the image reconstruction.

### *B. Single Moving Target*

The first simulation of our method shows a basic test case of a single target moving at a slower velocity of about 9 m/s towards the right. The scene at the initial time of  $s = 0$  is shown in Figure 6. We refer to this setup as Scene 1. Figure 6 also shows the reconstructed image when a hypothesized velocity of zero is used. This incorrect velocity assumption produces a smeared target in the reconstructed image, since echoes are received from multiple locations across the scene over the length of the aperture. Figure 7 shows a part of the entropy image over the range of hypothesized velocities from -20 m/s to 20 m/s. The minimum point in this entropy image corresponds to the true velocity. Finally, the image is reconstructed using the estimated true velocity, obtained from finding the minimum entropy point in the entropy image. This image is shown on the right in Figure 7, and displays the ideal result of perfect reconstruction with no error.

The second simulation uses a single moving target in the same starting location as the first simulation and moving towards the bottom right of the image with a much greater velocity of about [18.1, 18.1] m/s. In this situation, additional receivers were added to limit the amount of time necessary to collect the required data. We refer to this setup as Scene 2. Figure 8 on the left shows the plot of the entropy for hypothesized velocities of -50 m/s to 50 m/s in each direction of velocity. This plot shows a clear minimum entropy point at the true velocity of [18.1, 18.1] m/s. The reconstructed image is shown on the right side of this figure, which shows similar results to the first case.

### *C. Multiple Moving Targets*

The third simulation demonstrates the algorithm's performance for a scene with multiple targets. The original scene for this simulation is shown on the left in Figure 9. There are two moving targets, one in the top left moving

to the right at a velocity of 9 m/s and one in the bottom right moving towards the top left of the image traveling at about 12.8 m/s. In addition, there are two stationary targets; one is located just to the top right of the center of the scene and the other in the bottom left. We refer to this setup Scene 3. Figure 9 on the right shows the entropy for Scene 3. The three minimum points on the surface correspond to the true velocity of each of the two moving targets as well as the zero velocity. Figure 10 shows two of the reconstructed images corresponding to the velocity of the first target and the zero velocity, respectively. Figure 11 on the left shows the third hypothesized velocity reconstruction, which corresponds to the second moving target in the bottom right of the image. Accurate position reconstruction is obtained; however, with the multiple target case, we can see artifacts in each of the images resulting from the blurring of the incorrect targets. The method still reconstructs the true target at a much higher strength than the artifacts, however. Figure 11 on the right shows the cross-section of the horizontal row of the image containing the true target located in the bottom right corner. Here we can see that the amplitude of the target is much larger than the rest of the scene. To compare with the amplitude of a blurring artifact, a plot of the row containing the top right stationary target is shown in Figure 12. The maximum amplitude shown here is just under 0.5, which is about half of the amplitude of the focused target. Note that weak targets could be masked by stronger targets. However, for this to occur, the strong and weak targets must be close in position, and the smearing artifacts of the strong target must be in the direction of the weaker target.

#### *D. Multiple Moving Targets Embedded in Clutter*

Finally, in the fourth simulation we investigate the effects of clutter on the performance of the algorithm. We simulate a moving target in the top left of the scene moving towards the right at about 9 m/s. Clutter was added to the scene by using a Rayleigh distribution for the clutter amplitude as described in [63]. Although neither the forward model nor the image reconstruction method attempt to model or suppress clutter, we obtain acceptable results with a high enough Signal-to-Clutter Ratio (SCR). To test the sensitivity of velocity estimation, the peak SCR (the ratio between target strength and clutter strength) was varied from 0 to 36 dB with steps of 2 dB. A plot of velocity root-mean-square error versus SCR is shown in Figure 13. This plot portrays accurate estimation at higher SCR levels, but there is a decline in performance at around 18 dB. Until this point, we see a graceful degradation of performance, indicating a degree of robustness of method with respect to clutter. Below this SCR level, the clutter becomes too dominant for the algorithm to estimate the target velocity. The curve then flattens out again because of the natural upper bound set by the velocity search grid, since we use a finite range of hypothesized velocities.

## VII. CONCLUSION

This paper presents a method for image reconstruction and velocity estimation of a scene with moving targets using a network of passive receivers and non-cooperative sources of opportunity. Passive radar systems are an attractive solution because of their inherent cost, simplicity, and stealth advantages. Systems that are free of transmitters are cheaper to implement and harder to detect, which potentially increases the system's longevity. In addition, the

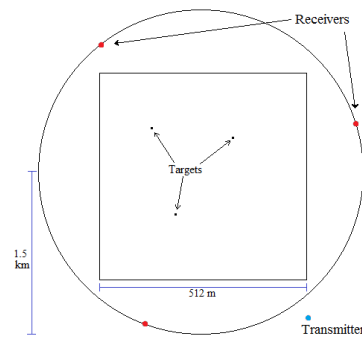


Fig. 5. Setup for the simulations. The receivers move in a circular trajectory with a radius of 11 km, while the transmitter is stationary outside of the scene. The scene size is  $[256 \times 256]$  m.

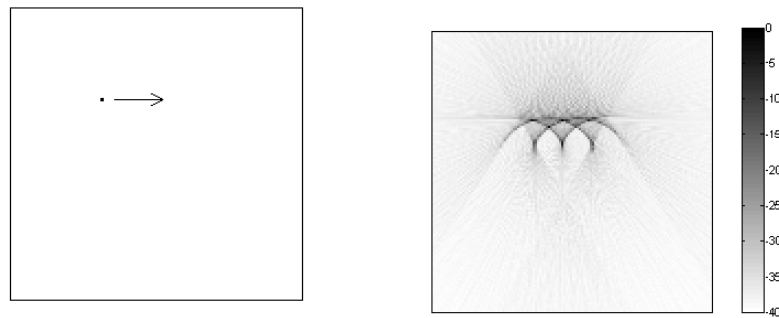


Fig. 6. Original setup of Scene 1 on the left along with the reconstruction on the right under the assumption of zero velocity. There is one moving target located in the upper left quadrant traveling towards the right at 1 m/s.

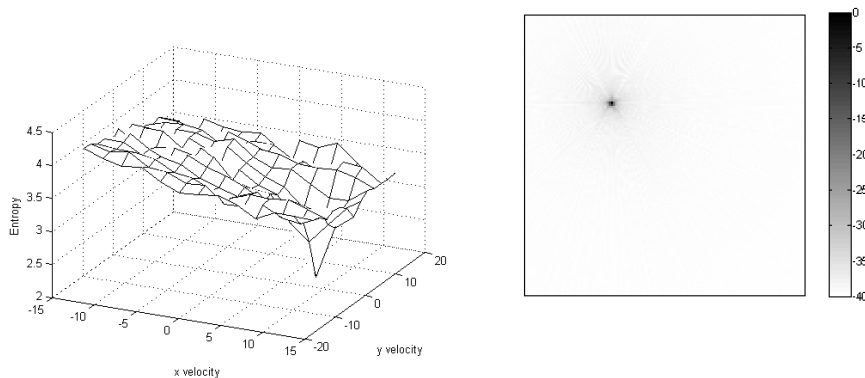


Fig. 7. The left figure shows the entropy associated with Scene 1 plotted as a function of hypothesized velocity. The minimum point (the darkest pixel) is at the correct target velocity, that is  $[1, 0]$  m/s. The image reconstruction corresponding to this hypothesized velocity is shown on the right.

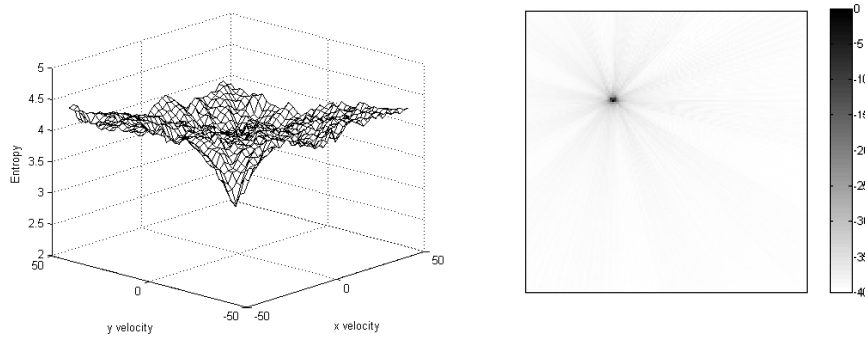


Fig. 8. The left figure shows the entropy associated with Scene 2 plotted as a function of the hypothesized velocity over the full range of -50 m/s to 50 m/s in each direction. The minimum point is at [18.1, -18.1] m/s, the velocity of the moving target. The right figure shows the reconstructed image for Scene 2 with the hypothesized velocity for set to the estimated velocity vector of [18.1, -18.1] from minimum entropy.

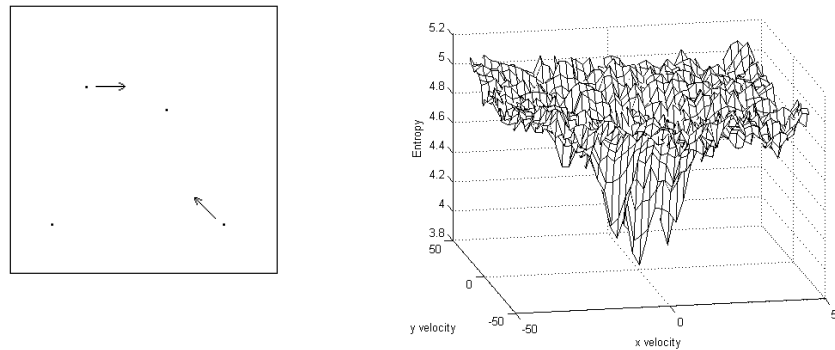


Fig. 9. Scene 3 is shown on the left. There are two moving targets, one located in the upper left quadrant moving towards the right at velocity 9 m/s and one in the lower right quadrant moving towards the top left at velocity of about 12.8 m/s. There are also two stationary targets, one to the top right of the center of the scene and one in the bottom left. The right figure shows the entropy image associated with Scene 3. The minimum points of the image correspond to the true velocity of each of the moving targets as well as the zero velocity.

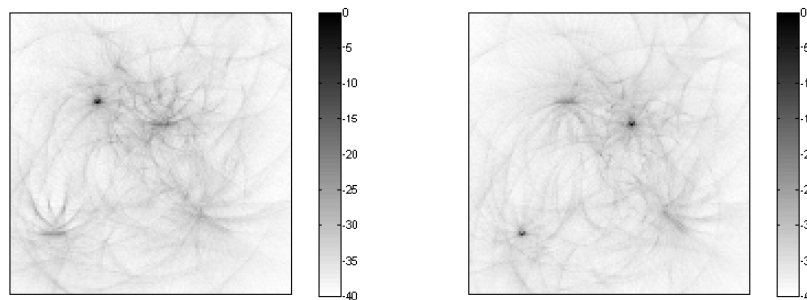


Fig. 10. The reconstructed images for Scene 3 with the hypothesized velocity set to each of two of the three minimum points on the velocity image, the [9, 0] and [0, 0] velocities, respectively. Each image shows the focused target corresponding to the hypothesized velocity.

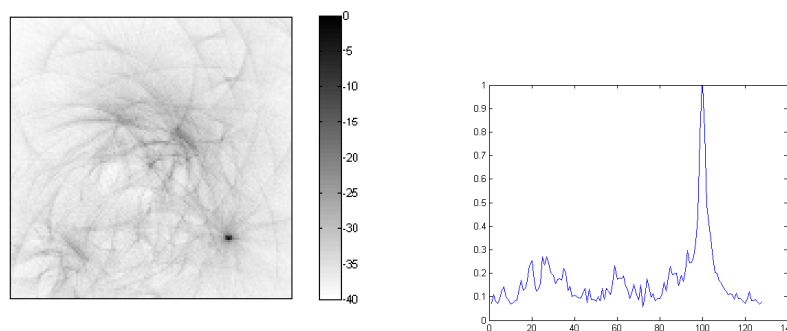


Fig. 11. The left figure shows the reconstruction for the third minimum point in the entropy image with a hypothesized velocity of  $[-9, 9]$  m/s. Shown on the right is the horizontal cross-section of this reconstruction along the row containing the moving target. One can see here that the target still stands out above the blurring artifacts from the other moving targets.

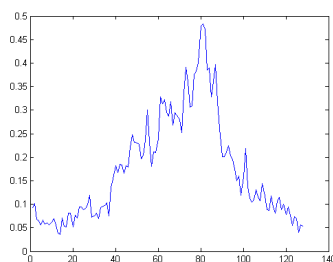


Fig. 12. A plot of the top right stationary target in the third reconstructed image, focused for the bottom right moving target. The maximum amplitude shown here is just under 0.5, which is about half of the amplitude of the focused target.

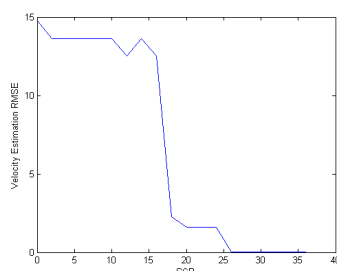


Fig. 13. This plot shows the resulting RMSE for velocity estimation at various levels of SCRs. At higher SCR levels we still obtain accurate velocity estimation with a steady decline in performance as SCR is reduced.

problem of imaging moving targets is important to address, since targets of interest are often mobile, and without special processing they appear smeared and unfocused in the reconstructed image.

This paper introduces a novel forward model and an FBP-type inversion method for passive imaging of a moving scene. The forward model is based on the correlation of received signals from different receivers and includes a phase term due to moving target displacement. We defined a backprojection operator and showed that if the true velocities of targets are used, our backprojection operator focuses the targets in the reconstructed radiance images. We then used a range of hypothesized velocities and reconstructed a stack of radiance images, each one corresponding to a hypothesized velocity. We used entropy as a metric to measure the degree of focus in reconstructed images. The minimum entropy analysis yields the velocity estimate for each target as well as its corresponding image.

Our method relies on repeated use of backprojection operator which can be implemented efficiently by using fast backprojection algorithms or fast Fourier integral operator computation methods and by utilizing parallel processing on graphics processing units.

We performed numerical simulations to demonstrate the viability of our method for single and multiple moving target scenarios. While our method does not explicitly consider clutter, our simulation study shows that entropy is a robust metric for estimating velocity at relatively low SCR levels. Additionally, since our image reconstruction method is backprojection-based, the image formation method holds in the presence of additive measurement noise under the assumption that the noise is uncorrelated from one receiver to another [64]. When the noise and clutter are correlated, the results can be further improved by taking into account the statistics of the noise and clutter as in [65].

In this work we assumed that all targets were isotropic scatterers. However, when a wide enough aperture angle is used, this assumption is no longer valid, and one may wish to extend the model to account for anisotropic scatterers. This can be done by creating small subapertures defined by a small error in the Fourier vector, so that the isotropic assumption is valid for each subaperture. This technique is described in more detail in [66].

This technique is designed for imaging moving targets located on the ground, but the technique can be extended to image airborne targets in a straightforward manner. In that case, however, the number of unknowns would increase, both in position and velocity. As a result, the two-dimensional position-velocity ambiguities (as described in Part 2) would extend to three-dimensional ambiguities. Additionally, the computational complexity would significantly increase.

In Part 2 [67], we analyze the performance of our method. We present position (radiance) and velocity resolution analysis and introduce a theory to analyze and predict smearing artifacts in the reconstructed radiance images due to incorrect velocity information.

## APPENDIX A

### DERIVATION OF THE ISO-DOPPLER CONTOURS

The iso-Doppler contours are represented by the set of points  $(\mathbf{x}, v)$  that satisfy

$$\partial_s R_{ij}(\mathbf{x}, s) + \partial_s B_{ij}(\mathbf{x}, \mathbf{v}, s) = C_D, \quad (67)$$

where  $C_D$  is a constant.

Differentiating the  $R_{ij}(\mathbf{x}, s)$  and  $B_{ij}(\mathbf{x}, \mathbf{v}, s)$  terms with respect to  $s$  yields

$$\begin{aligned} & (\widehat{\mathbf{x} - \boldsymbol{\gamma}_i(s)}) \cdot (\mathbf{v} - \dot{\boldsymbol{\gamma}}_i(s)) - (\widehat{\mathbf{x} - \boldsymbol{\gamma}_j(s)}) \cdot (\mathbf{v} - \dot{\boldsymbol{\gamma}}_j(s)) \\ & - \frac{\dot{\boldsymbol{\gamma}}_i(s)s}{|\mathbf{x} - \boldsymbol{\gamma}_i(s)|} \cdot [\mathbf{v} - (\widehat{\mathbf{x} - \boldsymbol{\gamma}_i(s)})((\widehat{\mathbf{x} - \boldsymbol{\gamma}_i(s)}) \cdot \mathbf{v})] \\ & + \frac{\dot{\boldsymbol{\gamma}}_j(s)s}{|\mathbf{x} - \boldsymbol{\gamma}_j(s)|} \cdot [\mathbf{v} - (\widehat{\mathbf{x} - \boldsymbol{\gamma}_j(s)})((\widehat{\mathbf{x} - \boldsymbol{\gamma}_j(s)}) \cdot \mathbf{v})]. \end{aligned} \quad (68)$$

We then define the  $\mathbf{v}^\perp$  vectors as

$$\mathbf{v}_i^\perp = \mathbf{v} - (\widehat{\mathbf{x} - \boldsymbol{\gamma}_i(s)})[(\widehat{\mathbf{x} - \boldsymbol{\gamma}_i(s)}) \cdot \mathbf{v}] \quad (69)$$

$$\mathbf{v}_j^\perp = \mathbf{v} - (\widehat{\mathbf{x} - \boldsymbol{\gamma}_j(s)})[(\widehat{\mathbf{x} - \boldsymbol{\gamma}_j(s)}) \cdot \mathbf{v}] \quad (70)$$

and substitute into the derivative computed in (68) to obtain

$$\begin{aligned} C_D &= (\widehat{\mathbf{x} - \boldsymbol{\gamma}_i(s)}) \cdot (\mathbf{v} - \dot{\boldsymbol{\gamma}}_i(s)) - (\widehat{\mathbf{x} - \boldsymbol{\gamma}_j(s)}) \cdot (\mathbf{v} - \dot{\boldsymbol{\gamma}}_j(s)) \\ & - \frac{\dot{\boldsymbol{\gamma}}_i(s)s}{|\mathbf{x} - \boldsymbol{\gamma}_i(s)|} \cdot \mathbf{v}_i^\perp + \frac{\dot{\boldsymbol{\gamma}}_j(s)s}{|\mathbf{x} - \boldsymbol{\gamma}_j(s)|} \cdot \mathbf{v}_j^\perp. \end{aligned} \quad (71)$$

## APPENDIX B

### DERIVATION OF THE $\Xi_{ij}$ VECTOR

To derive the  $\Xi_{ij}$  vector, we let

$$\Xi_{ij}(s, \mathbf{x}', \mathbf{v}) = \nabla_{\mathbf{x}}[-R_{ij}(\mathbf{x}, s) - B_{ij}(\mathbf{x}, \mathbf{v}, s)]|_{\mathbf{x}=\mathbf{x}'}. \quad (72)$$

The gradient of the first term is equivalent to the result in [6] and is found to be

$$\begin{aligned} \nabla_{\mathbf{x}} R_{ij}(\mathbf{x}, s) &= \nabla_{\mathbf{x}}[|\mathbf{x} - \boldsymbol{\gamma}_i(s)| - |\mathbf{x} - \boldsymbol{\gamma}_j(s)|] \\ &= D\psi[(\widehat{\mathbf{x} - \boldsymbol{\gamma}_i(s)}) - (\widehat{\mathbf{x} - \boldsymbol{\gamma}_j(s)})] \end{aligned} \quad (73)$$

where

$$D\psi = \begin{bmatrix} 1 & 0 & \partial\psi(\mathbf{x})/\partial x_1 \\ 0 & 1 & \partial\psi(\mathbf{x})/\partial x_2 \end{bmatrix} \quad (74)$$

The gradient of the second term containing the moving target motion is found by computing the gradient of each term:

$$\begin{aligned} \nabla_{\mathbf{x}}[(\widehat{\mathbf{x} - \boldsymbol{\gamma}_i(s)}) \cdot \mathbf{v}s] &= \nabla_{\mathbf{x}} \left[ \frac{(\mathbf{x} - \boldsymbol{\gamma}_i(s)) \cdot \mathbf{v}s}{|\mathbf{x} - \boldsymbol{\gamma}_i(s)|} \right] \\ &= \frac{\nabla_{\mathbf{x}}[(\mathbf{x} - \boldsymbol{\gamma}_i(s)) \cdot \mathbf{v}s] - \nabla_{\mathbf{x}}|\mathbf{x} - \boldsymbol{\gamma}_i(s)|[(\mathbf{x} - \boldsymbol{\gamma}_i(s)) \cdot \mathbf{v}s]}{|\mathbf{x} - \boldsymbol{\gamma}_i(s)|^2} \\ &= \frac{\nabla_{\mathbf{x}}[(\mathbf{x} - \boldsymbol{\gamma}_i(s)) \cdot \mathbf{v}s] - D\psi(\widehat{\mathbf{x} - \boldsymbol{\gamma}_i(s)})[(\mathbf{x} - \boldsymbol{\gamma}_i(s)) \cdot \mathbf{v}s]}{|\mathbf{x} - \boldsymbol{\gamma}_i(s)|^2} \end{aligned} \quad (75)$$

Note that the velocity vector is of the form

$$\mathbf{v} = [v_1, v_2, \nabla_{\mathbf{x}}\psi(\mathbf{x}) \cdot \mathbf{v}], \quad (76)$$

so we can find the gradient of the first term in (75) as

$$\begin{aligned} \nabla_{\mathbf{x}}[(\mathbf{x} - \gamma_i(s)) \cdot \mathbf{v}s] &= \nabla_{\mathbf{x}}[(x_1 - \gamma_i^1(s))v_1 + (x_2 - \gamma_i^2(s))v_2 \\ &\quad + (x_3 - \gamma_i^3(s))\nabla_{\mathbf{x}}\psi(\mathbf{x}) \cdot \mathbf{v}]s \\ &= \begin{bmatrix} v_1 + \partial_{x_1}\psi(\mathbf{x})v_3s \\ v_2 + \partial_{x_2}\psi(\mathbf{x})v_3s \end{bmatrix} \\ &\quad + \begin{bmatrix} \frac{\partial^2}{\partial x_1^2} & \frac{\partial^2}{\partial x_1\partial x_2} \\ \frac{\partial^2}{\partial x_1\partial x_2} & \frac{\partial^2}{\partial x_2^2} \end{bmatrix} \psi(\mathbf{x}) \cdot \begin{bmatrix} v_1 \\ v_2 \end{bmatrix} \cdot (\psi(\mathbf{x}) - \gamma_i^3(s))s \\ &= D\psi\mathbf{v}s + \partial_{\mathbf{x}}^2\psi(\mathbf{x}) \cdot \mathbf{v}(\psi(\mathbf{x}) - \gamma_i^3(s))s, \end{aligned} \quad (77)$$

where

$$\partial_{\mathbf{x}'}^2 = \begin{bmatrix} \partial^2/\partial x_1'^2 & \partial^2/\partial x_1'x_2' \\ \partial^2/\partial x_2'x_1' & \partial^2/\partial x_2'^2 \end{bmatrix}. \quad (78)$$

Plugging this result back into (75), we obtain the final form of the  $\Xi_{ij}$  vector after normalizing with the range, substituting in the  $\mathbf{v}_i^\perp$ , repeating the steps with the  $j$  receiver, and finally substituting  $\mathbf{x}'$  for  $\mathbf{x}$ :

$$\begin{aligned} \Xi_{ij}(s, \mathbf{x}', \mathbf{v}) &= -D\psi \cdot [(\widehat{\mathbf{x}' - \gamma_i(s)}) - (\widehat{\mathbf{x}' - \gamma_j(s)})] \\ &\quad - \frac{D\psi \cdot \mathbf{v}_i^\perp s + \partial_{\mathbf{x}'}^2\psi(\mathbf{x}') \cdot \mathbf{v}(\psi(\mathbf{x}') - \gamma_i^3(s))s}{|\mathbf{x}' - \gamma_i(s)|} \\ &\quad + \frac{D\psi \cdot \mathbf{v}_j^\perp s + \partial_{\mathbf{x}'}^2\psi(\mathbf{x}') \cdot \mathbf{v}(\psi(\mathbf{x}') - \gamma_j^3(s))s}{|\mathbf{x}' - \gamma_j(s)|} \end{aligned} \quad (79)$$

#### REFERENCES

- [1] H.D. Griffiths and C.J. Baker, "Passive coherent location radar systems. part 1: performance prediction," *Radar, Sonar and Navigation, IEE Proceedings -*, vol. 152, no. 3, pp. 153 – 159, june 2005.
- [2] C.J. Baker, H.D. Griffiths, and I. Papoutsis, "Passive coherent location radar systems. part 2: waveform properties," *Radar, Sonar and Navigation, IEE Proceedings -*, vol. 152, no. 3, pp. 160 – 168, june 2005.
- [3] A. D. Lanterman and Jr. D. C. Munson, "Deconvolution techniques for passive radar imaging," *Algorithms for Synthetic Aperture Radar Imagery IX, Proc. SPIE*, vol. 4727, pp. 166–177, 2002.
- [4] M. Çetin and A.D. Lanterman, "Region-enhanced imaging for sparse-aperture passive radar," *Algorithms for Synthetic Aperture Radar Imagery XI, Proc. SPIE*, vol. 5427, 2004.
- [5] Y. Wu and Jr. D. C. Munson, "Multistatic synthetic aperture imaging of aircraft using reflected television signals," *Algorithms for Synthetic Aperture Radar Imagery VIII, Proc. SPIE*, vol. 4382, 2001.
- [6] C. E. Yarman and B. Yazıcı, "Synthetic aperture hitchhiker imaging," *IEEE Transactions on Imaging Processing*, vol. 17(11), pp. 2156–2173, 2008.
- [7] C. E. Yarman, L. Wang, and B. Yazıcı, "Doppler synthetic aperture hitchhiker imaging," *Inverse Problems*, vol. 26 (065006), 2010.
- [8] L. Wang, C.E. Yarman, et al., "Doppler-hitchhiker: A novel passive synthetic aperture radar using ultranarrowband sources of opportunity," *Geoscience and Remote Sensing, IEEE Transactions on*, , no. 99, pp. 1–17, 2011.
- [9] R.W. Deming, "Along-track interferometry for simultaneous SAR and GMTI: application to gotcha challenge data," in *Proceedings of SPIE*, 2011, vol. 8051, p. 80510P.

- [10] V.C. Chen, "Time-frequency analysis of SAR images with ground moving targets," in *Proceedings of SPIE*, 1998, vol. 3391, p. 295.
- [11] MJ Minardi, LA Gorham, and EG Zelnio, "Ground moving target detection and tracking based on generalized SAR processing and change detection," in *Proceedings of SPIE*, 2005, vol. 5808, p. 156.
- [12] D.E. Hack and M.A. Saville, "Analysis of SAR moving grid processing for focusing and detection of ground moving targets," in *Proceedings of SPIE*, 2011, vol. 8051, p. 80510S.
- [13] S. Barbarossa, "Detection and imaging of moving objects with synthetic aperture radar. 1. optimal detection and parameter estimation theory," in *Radar and Signal Processing, IEE Proceedings F*, IET, 1992, vol. 139, pp. 79–88.
- [14] M. Kirscht, "Detection and imaging of arbitrarily moving targets with single-channel SAR," in *Radar, Sonar and Navigation, IEE Proceedings-*, IET, 2003, vol. 150, pp. 7–11.
- [15] M. Stuff, M. Biancalana, G. Arnold, and J. Garbarino, "Imaging moving objects in 3D from single aperture synthetic aperture radar," in *Radar Conference, 2004. Proceedings of the IEEE*. IEEE, 2004, pp. 94–98.
- [16] F. Zhou, R. Wu, M. Xing, and Z. Bao, "Approach for single channel SAR ground moving target imaging and motion parameter estimation," *Radar, Sonar & Navigation, IET*, vol. 1, no. 1, pp. 59–66, 2007.
- [17] RP Perry, RC Dipietro, and RL Fante, "SAR imaging of moving targets," *Aerospace and Electronic Systems, IEEE Transactions on*, vol. 35, no. 1, pp. 188–200, 1999.
- [18] S. Zhu, G. Liao, Y. Qu, Z. Zhou, and X. Liu, "Ground moving targets imaging algorithm for synthetic aperture radar," *Geoscience and Remote Sensing, IEEE Transactions on*, vol. 49, no. 1, pp. 462–477, 2011.
- [19] Ling Wang and Birsen Yazici, "Ground moving target imaging using ultranarrowband continuous wave synthetic aperture radar," 2013.
- [20] Ling Wang and Birsen Yazici, "Bistatic synthetic aperture radar imaging of moving targets using ultra-narrowband continuous waveforms," *arXiv preprint arXiv:1302.5340*, 2013.
- [21] B Dawidowicz, P Samczynski, M Malanowski, J Misiurewicz, and KS Kulpa, "Detection of moving targets with multichannel airborne passive radar," *Aerospace and Electronic Systems Magazine, IEEE*, vol. 27, no. 11, pp. 42–49, 2012.
- [22] P. Krysiak and K. Kulpa, "The use of a GSM-based passive radar for sea target detection," in *Radar Conference (EuRAD), 2012 9th European*. IEEE, 2012, pp. 142–145.
- [23] M. M. Chitgarha, M. N. Majd, M. Radmard, and M. M. Nayebi, "Choosing the position of the receiver in a MISO passive radar system," in *Radar Conference (EuRAD), 2012 9th European*. IEEE, 2012, pp. 318–321.
- [24] J. Brown, K. Woodbridge, H. Griffiths, A. Stove, and S. Watts, "Passive bistatic radar experiments from an airborne platform," *Aerospace and Electronic Systems Magazine, IEEE*, vol. 27, no. 11, pp. 50–55, november 2012.
- [25] HD Griffiths and NRW Long, "Television-based bistatic radar," *Communications, Radar and Signal Processing, IEE Proceedings F*, vol. 133, no. 7, pp. 649–657, 1986.
- [26] P.E. Howland, "Target tracking using television-based bistatic radar," in *Radar, Sonar and Navigation, IEE Proceedings-*, IET, 1999, vol. 146, pp. 166–174.
- [27] C.J. Coleman, R.A. Watson, and H. Yardley, "A practical bistatic passive radar system for use with DAB and DRM illuminators," in *Radar Conference, 2008. RADAR '08. IEEE*, may 2008, pp. 1–6.
- [28] P.E. Howland, D. Maksimiuk, and G. Reitsma, "FM radio based bistatic radar," *Radar, Sonar and Navigation, IEE Proceedings -*, vol. 152, no. 3, pp. 107–115, june 2005.
- [29] L. Wang and B. Yazici, "Passive imaging of moving targets using sparse distributed apertures," *SIAM Journal on Imaging Sciences*, vol. 5, no. 3, pp. 769–808, 2012.
- [30] J.E. Palmer and S.J. Searle, "Evaluation of adaptive filter algorithms for clutter cancellation in passive bistatic radar," in *Radar Conference (RADAR), 2012 IEEE*. IEEE, 2012, pp. 0493–0498.
- [31] DKP Tan, H. Sun, Y. Lu, M. Lesturgie, and HL Chan, "Passive radar using global system for mobile communication signal: theory, implementation and measurements," in *Radar, Sonar and Navigation, IEE Proceedings-*, IET, 2005, vol. 152, pp. 116–123.
- [32] V. Koch and R. Westphal, "New approach to a multistatic passive radar sensor for air/space defense," *Aerospace and Electronic Systems Magazine, IEEE*, vol. 10, no. 11, pp. 24–32, 1995.
- [33] KS Kulpa, "Multi-static entirely passive detection of moving targets and its limitations," in *Radar, Sonar and Navigation, IEE Proceedings-*, IET, 2005, vol. 152, pp. 169–173.

- [34] D. Poullin, "Passive detection using digital broadcasters (DAB, DVB) with COFDM modulation," in *Radar, Sonar and Navigation, IEE Proceedings-*. IET, 2005, vol. 152, pp. 143–152.
- [35] C. Mikhail, K. Kurt, and N. David, "Bistatic synthetic aperture radar with non-cooperative LEOS based transmitter," in *Geoscience and Remote Sensing Symposium, 2000. Proceedings. IGARSS 2000. IEEE 2000 International*. IEEE, 2000, vol. 2, pp. 861–862.
- [36] J. Homer, K. Kubik, B. Mojarrabi, ID Longstaff, E. Donskoi, and M. Cherniakov, "Passive bistatic radar sensing with LEOS based transmitters," in *Geoscience and Remote Sensing Symposium, 2002. IGARSS'02. 2002 IEEE International*. IEEE, 2002, vol. 1, pp. 438–440.
- [37] M. Cherniakov, R. Saini, R. Zuo, and M. Antoniou, "Space surface bistatic SAR with space-borne non-cooperative transmitters," in *Radar Conference, 2005. EURAD 2005. European*. IEEE, 2005, pp. 9–12.
- [38] X. He, T. Zeng, and M. Cherniakov, "Signal detectability in SS-BSAR with GNSS non-cooperative transmitter," in *Radar, Sonar and Navigation, IEE Proceedings-*. IET, 2005, vol. 152, pp. 124–132.
- [39] J. Garnier, G. Papanicolaou, et al., "Passive sensor imaging using cross correlations of noisy signals in a scattering medium," *Siam J. Imaging Sciences*, vol. 2, pp. 396–437, 2009.
- [40] Anthony J Weiss, "Direct geolocation of wideband emitters based on delay and doppler," *Signal Processing, IEEE Transactions on*, vol. 59, no. 6, pp. 2513–2521, 2011.
- [41] Joseph R Guerci, *Space-time adaptive processing for radar*, Artech House, 2003.
- [42] Richard Klemm, *Principles of space-time adaptive processing*, Number 159-162. IET, 2002.
- [43] James Ward, "Space-time adaptive processing for airborne radar," 1998.
- [44] M. Martorella, F. Berizzi, and B. Haywood, "Contrast maximisation based technique for 2-D ISAR autofocusing," in *Radar, Sonar and Navigation, IEE Proceedings-*. IET, 2005, vol. 152, pp. 253–262.
- [45] C.V. Jakowatz Jr, D.E. Wahl, and P.H. Eichel, "Refocus of constant-velocity moving targets in synthetic aperture radar imagery," in *Proceedings of SPIE*, 1998, vol. 3370, p. 85.
- [46] L. Xi, L. Guosui, and J. Ni, "Autofocusing of ISAR images based on entropy minimization," *Aerospace and Electronic Systems, IEEE Transactions on*, vol. 35, no. 4, pp. 1240–1252, 1999.
- [47] D. Atkinson, D.L.G. Hill, P.N.R. Stoye, P.E. Summers, and S.F. Keevil, "Automatic correction of motion artifacts in magnetic resonance images using an entropy focus criterion," *Medical Imaging, IEEE Transactions on*, vol. 16, no. 6, pp. 903–910, 1997.
- [48] Ali F Yegulalp, "Minimum entropy sar autofocus," in *Adaptive Sensor Array Processing (ASAP) Workshop, MIT Lincoln Laboratory, Lexington, MA*, 1999.
- [49] JR Fienup, "Synthetic-aperture radar autofocus by maximizing sharpness," *Optics Letters*, vol. 25, no. 4, pp. 221–223, 2000.
- [50] JR Fienup and JJ Miller, "Aberration correction by maximizing generalized sharpness metrics," *JOSA A*, vol. 20, no. 4, pp. 609–620, 2003.
- [51] Thomas J Kragh, "Monotonic iterative algorithm for minimum-entropy autofocus," in *Adaptive Sensor Array Processing (ASAP) Workshop, (June 2006)*, 2006.
- [52] L. Demanet, M. Ferrara, N. Maxwell, J. Poulson, and L. Ying, "A butterfly algorithm for synthetic aperture radar imaging," *Session 4P1 Dimensionality Reduction of Large Scale forward and Inverse EM Problems*, p. 638, 2010.
- [53] K. Duman and B. Yazici, "Bi-static synthetic aperture radar imaging of moving targets," *To be submitted, SIAM Journal on Imaging Sciences*.
- [54] H.H. Barrett, K.J. Myers, and S. Rathee, *Foundations of image science*, vol. 44, Wiley-Interscience, 2004.
- [55] J.F. Treves, *Introduction to Pseudodifferential and Fourier Integral Operators Volume 2: Fourier Integral Operators*, vol. 2, Springer, 1980.
- [56] B. Yazici and V. Krishnan, "Microlocal analysis in imaging," Aug. 2010.
- [57] S.M. Kay, "Fundamentals of statistical signal processing, volume II: Detection theory," *Upper Saddle River (New Jersey)*, vol. 7, 1998.
- [58] John W McCorkle and Martin Rofheart, "Order  $n^2 \log(n)$  backprojector algorithm for focusing wide-angle wide-bandwidth arbitrary-motion synthetic aperture radar," in *Aerospace/Defense Sensing and Controls*. International Society for Optics and Photonics, 1996, pp. 25–36.
- [59] L.M.H. Ulander, H. Hellsten, and G. Stenstrom, "Synthetic-aperture radar processing using fast factorized back-projection," *Aerospace and Electronic Systems, IEEE Transactions on*, vol. 39, no. 3, pp. 760–776, 2003.

- [60] S. Nilsson and L.E. Andersson, "Application of fast back-projection techniques for some inverse problems of synthetic aperture radar," in *Society of Photo-Optical Instrumentation Engineers (SPIE) Conference Series*, 1998, vol. 3370, pp. 62–72.
- [61] E. Candes, L. Demanet, and L. Ying, "Fast computation of fourier integral operators," *SIAM Journal on Scientific Computing*, vol. 29, no. 6, pp. 2464–2493, 2007.
- [62] E. Candès, L. Demanet, and L. Ying, "A fast butterfly algorithm for the computation of fourier integral operators," *Multiscale Modeling & Simulation*, vol. 7, no. 4, pp. 1727–1750, 2009.
- [63] D.A. Shnidman, "Generalized radar clutter model," *Aerospace and Electronic Systems, IEEE Transactions on*, vol. 35, no. 3, pp. 857–865, 1999.
- [64] K Voccola, B Yazici, M Ferrara, and M Cheney, "On the relationship between the generalized likelihood ratio test and backprojection for synthetic aperture radar imaging," in *SPIE Defense, Security, and Sensing*. International Society for Optics and Photonics, 2009, pp. 73350I–73350I.
- [65] B. Yazici, M. Cheney, and C.E. Yarman, "Synthetic-aperture inversion in the presence of noise and clutter," *Inverse Problems*, vol. 22, no. 5, pp. 1705, 2006.
- [66] V Krishnan, J Swoboda, Can Evren Yarman, and Birsen Yazici, "Multistatic synthetic aperture radar image formation," *Image Processing, IEEE Transactions on*, vol. 19, no. 5, pp. 1290–1306, 2010.
- [67] S. Wacks and B. Yazici, "Passive synthetic aperture hitchhiker imaging of ground moving targets - part 2: Performance analysis," *In review Image Processing, IEEE Transactions on*.



**Steven Wacks** Steven Wacks received the BS degree in Electrical Engineering and Computer Science in 2006 from Rensselaer Polytechnic Institute.

He is currently pursuing his Ph.D. in Electrical Engineering at Rensselaer Polytechnic Institute. His research interests include radar, imaging, and signal processing.



**Birsen Yazici** Birsen Yazici received BS degrees in Electrical Engineering and Mathematics in 1988 from Bogazici University, Istanbul Turkey and MS and Ph.D. degrees in Mathematics and Electrical Engineering both from Purdue University, W. Lafayette IN, in 1990 and 1994, respectively. From September 1994 until 2000, she was a research engineer at General Electric Company Global Research Center, Schenectady NY. During her tenure in industry, she worked on radar, transportation, industrial and medical imaging systems. From 2001 to June 2003, she was an assistant professor at Drexel University, Electrical and Computer Engineering Department. In Fall 2003, she joined Rensselaer Polytechnic Institute where she is currently a full professor in the Department of Electrical, Computer and Systems

Engineering and in the Department of Biomedical Engineering.

Prof. Yazici's research interests span the areas of statistical signal processing, inverse problems in imaging, image reconstruction, biomedical optics, radar and X-ray imaging. From 2008 to 2012, she was an associate editor for the IEEE Transactions on Image Processing. She currently serves as an associate editor for SIAM Journal on Imaging Science. She is the recipient of the Rensselaer Polytechnic Institute 2007 and 2013 School of Engineering Research Excellence Awards. She holds 11 US patents.